Available online at www.sciencedirect.com
ScienceDirect
Trans. Nonferrous Met. Soc. China 32(2022) 639−656
Transactions of Nonferrous Metals Society of China
www.tnmsc.cn

# Failure behavior of horseshoe-shaped tunnel in hard rock under high stress: Phenomenon and mechanisms

Hao WU[1], Guo-yan ZHAO[2], Shao-wei MA[2]

1. School of Mines, China University of Mining and Technology, Xuzhou 221116, China;
2. School of Resources and Safety Engineering, Central South University, Changsha 410083, China

Received 5 November 2020; accepted 31 July 2021

**Abstract:** A particle flow code (PFC) was first applied to examining the mechanical response of a horseshoe-shaped opening in prismatic rock models under biaxial compression. Next, an improved complex variable method was proposed to derive the stress distribution around the opening. Lastly, a case study of tunnel failure caused by rock burst in Jinping II Hydropower Station was further analyzed and discussed. The results manifest that a total of four types of cracks occur around the opening under low lateral confining stress, namely, the primary-tensile cracks on the roof-floor, sidewall cracks on the sidewalls, secondary-tensile cracks on the corners and shear cracks along the diagonals. As the confining stress increases, the tensile cracks gradually disappear whilst the spalling failure becomes severe. Overall, the failure phenomenon of the modelled tunnel agrees well with that of the practical headrace tunnel, and the crack initiation mechanisms can be clearly clarified by the analytical stress distribution.

**Key words:** horseshoe-shaped tunnel; fracture behavior; rock burst; stress distribution; complex variable method; particle flow code

## 1 Introduction

Natural rock mass at depth is subjected to geo-stress due to the weight of the overlying strata and the tectonic movement of the earth's crust [1]. When a tunnel is excavated in the stressed rock, the stresses around the opening are redistributed, depending on the geologic structure, tunnel shape and in-situ stress [2,3]. Research manifests that, as the buried depth of the tunnel grows, the frequency of rock disasters, such as rock burst, water gushing-out and tunnel collapse, increases significantly [4−6]. Essentially, the deformation, burst and failure of the host rock are driven by the excavation-induced stresses. Thus, figuring out the stress distribution near the tunnel is necessary and meaningful to understand the failure mechanism.

Up to now, extensive attempts have been made on the measurement of rock stress. For example, FIGUEIREDO et al [7] successfully determined the surface stress around a tunnel by using large flat jack test method, and provided formulas for normal and shear stresses. GE and HOU [8] proposed borehole wall stress relief method and designed a set of instruments to monitor the orientations and magnitudes of the maximum, intermediate and minimum principal stresses near a tunnel of Jinping II Hydropower Station. CAI et al [9] employed an improved hydraulic fracturing technique along with modified test equipment for measuring the geo-stress in a 1000 m coal mine. By stress cell and extensometer, KAISER et al [10] explored the influence of mining-induced stress change on excavation stability. OUYANG et al [11] also utilized multiple MC-type bore-hole stress gauges

**Corresponding author:** Shao-wei MA, Tel: +86-15200824623, E-mail: mashaowei@csu.edu.cn
DOI: 10.1016/S1003-6326(22)65822-9

to study the induced stress distribution around a stope in an iron mine. Besides, QIU et al [12] presented electromagnetic radiation (EMR) stress measurement technique and applied it to a roadway in Nuodong coal mine. Based on the micro-seismic monitoring technique, MAXWELL and YOUNG [13] further developed sequential imaging method for analyzing the variation of excavation-induced stress around a roadway. Note that the above methods could only be used to measure the stress state of a certain point, and thus both the cost and workload will increase accordingly if the entire stress field is obtained. Additionally, photo-elastic test and physical model experiment were conducted to investigate the evolution of surrounding stress around an opening [14,15]. Moreover, a series of commercial software based on finite, discrete and boundary element methods have been developed to simulate the mechanical response caused by tunnel excavation. Since the constitutive model, element or particle size, material parameter and boundary condition all have remarkable effects on the numerical results, it is extremely time consuming and troublesome to determine the required parameters for numerical modelling [16−19].

By contrast, theoretical study on the excavation-induced stress has received relatively little attention. The reason is that it is quite arduous to solve the indispensable Airy stress function using elasticity theory, especially for the complex shaped openings. As an effective tool, complex variable approach is widely used for solving the surrounding stresses of non-circular tunnels such as square, rectangular, semi-circular, inverted U-shaped, and trapezoidal [20−25]. Nevertheless, in regard to the horseshoe-shaped tunnels that are widespread in civil and hydraulic engineering, limited information regarding the surrounding stress distribution and fracture response is reported in previous literature [2]. As a result, the deformation and failure mechanism of this type of tunnel have not been thoroughly grasped. Therefore, in this work, we were encouraged to perform a numerical study on failure behavior of horseshoe-shaped tunnel under biaxial loading using a particle flow code (PFC) code, and then the stress distribution used to explain the fracture mechanism was derived via complex variable method together with a proposed shrinkage approximation algorithm.

## 2 Failure behavior of horseshoe-shaped tunnel

To deeply understand the failure behavior of horseshoe-shaped tunnel in rock engineering, it is essential to examine the crack development around the opening. Therefore, numerical study on the prismatic rock samples containing a horseshoe tunnel under biaxial compression with different confining stresses was conducted.

### 2.1 Determination of micro parameters for PFC modelling

Currently, it is universally accepted that discrete element software is particularly suitable for simulating the nonlinear mechanical behavior of discontinuous media [26]. In particular, PFC is popularly devoted to investigating the crack initiation, propagation and coalescence behavior of rock or rock-like materials under static or dynamic loads.

In PFC model, the medium is regarded as an aggregation of bonded circular or spherical rigid particles (balls) of different sizes, and the parallel-bond model is commonly selected for rock-like materials. As the macro-scale response of the model depends on the geometric and mechanical properties of the particles and the bonds, we need to calibrate the micro-contact parameters using trial-and-error method based on uniaxial compression test results. A block of sandstone with good homogeneity, taken from Linyi city in Shandong province of China, was applied to making rock specimens. The processed specimens used for tests contained three prismatic specimens with dimensions of 100 mm (length), 25 mm (width) and 150 mm (height), and three cylindrical specimens with sizes of 50 mm (diameter) × 100 mm (height). Correspondingly, the width and length of the PFC2D model were set as 100 and 150 mm, respectively. The tested mechanical parameters of the rock are: uniaxial compressive strength (102.61 MPa), elastic modulus (20.78 GPa) and Poisson's ratio (0.258). In contrast, the numerical results are 102.86 MPa, 22.02 GPa and 0.262, respectively. The stress−strain curves of the intact specimen and model under uniaxial compression are presented in Fig. 1. Since the sample models compressed by two discs are strictly two-dimensional,

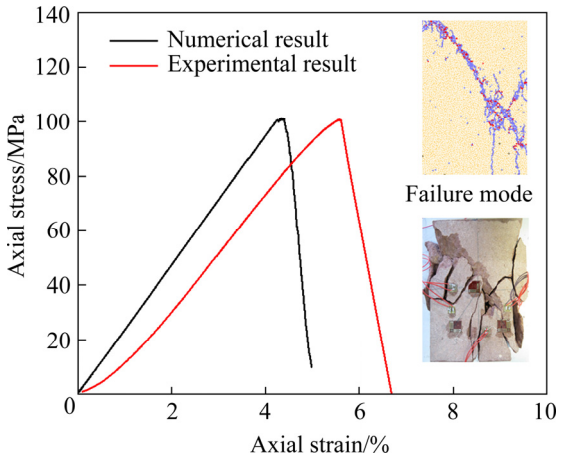


**Fig. 1** Experimental and numerical stress−strain curves and failure modes of intact specimens under uniaxial compression

no initial pores and cracks compaction stage appear during the modelling. Hence, the peak strain of the model is slightly smaller than that of the rock specimen. The calibrated micro-parameters of the model are shown in Table 1.

Besides, there are some other parameters, such as $\sigma_0$ (requested value of isotropic stress), $n_{\mathrm{fN}}$ (remaining floaters ratio), $\beta$ (wall normal stiffness multiplier) and $\bar{\lambda}$ (parallel-bond radius multiplier), which are set to defaults in modelling.

### 2.2 Strength and deformation properties

Considering that the long tunnel belongs to the plane strain problem, biaxial compression tests with five levels of confining stresses (0, 5, 10, 20 and 40 MPa) were carried out on rock model with a horseshoe-shaped opening. As a comparison, a model containing a circular opening with same cross-sectional area and the intact model were also studied. The deviator stress−strain curves of the three models are plotted in Fig. 2. Besides, the basic mechanical parameters of the models under different confining stresses, including the biaxial compressive strength $\sigma_{\mathrm{b}}$, elastic modulus $E$ and peak strain $\varepsilon_{\mathrm{p}}$, are listed in Table 2.

As can be seen in Fig. 2, the deformation process of the models under biaxial compressive loads can be divided into several stages according to the variation of the curves, that is, elastic stage, crack development stage and post-peak stage. With the increase of the axial strain, the deviator stress of the intact model under biaxial compression increases first before the peak stress and then decreases at the post-peak stage. Besides, both the peak stress and peak strain grow continuously with the increasing confining stress. The reason is that the confining stress suppresses the lateral deformation of the model. In contrast, as the confining stress rises, the peak deviator stress of the pre-holed models increases first, and then goes down. It is found that the curves fluctuate remarkably before the peak, which is induced by the unstable crack development around the openings. Thus, the crack development stage of the pre-holed models can be separated into two substages: stable crack development stage and unstable crack development stage. Also, all the curves become more and more gentle with the increase of the lateral stress in the post-peak stage, indicating that the brittleness of the models drops sharply.

Table 2 also gives detailed strength and deformation values. The biaxial compressive strength and elastic modulus basically mount with the confining stress. Compared with the intact model, the strength of the pre-holed models declines drastically by 25.16% to 33.77%. For the elastic modulus, the reduction rate is between 5.89% and 10.31%. It is also observed that the strength of

**Table 1** Main micro-scale parameters of parallel-bond model for rock model

| Parameter of particle | Value | Parameter of parallel-bond | Value |
|---|---|---|---|
| Ratio of largest-to-smallest ball radii, $R_{\max}/R_{\min}$ | 1.6 | Elastic modulus of each parallel bond, $\bar{E}_{\mathrm{c}}$/GPa | 19.46 |
| The smallest particle radius in sample, $R_{\min}$/mm | 0.40 | Ratio of parallel-bond normal to shear stiffness, $\bar{k}_{\mathrm{n}}/\bar{k}_{\mathrm{s}}$ | 2.17 |
| Particle density, $\rho$/(kg·m$^{-3}$) | 2925 | Mean value of normal strength, $\sigma_{\mathrm{c}}$/MPa | 84 |
| Elastic modulus at each particle−particle contact, $E_{\mathrm{c}}$/GPa | 19.46 | Mean value of shear strength, $\tau_{\mathrm{c}}$/MPa | 84 |
| Ratio of particle normal to shear stiffness, $k_{\mathrm{n}}/k_{\mathrm{s}}$ | 2.17 | Standard deviation of normal strength, $\bar{\sigma}_{\mathrm{c}}$/MPa | 0.50 |
| Particle friction coefficient, $\mu$ | 0.10 | Standard deviation of shear strength, $\bar{\tau}_{\mathrm{c}}$/MPa | 0.50 |

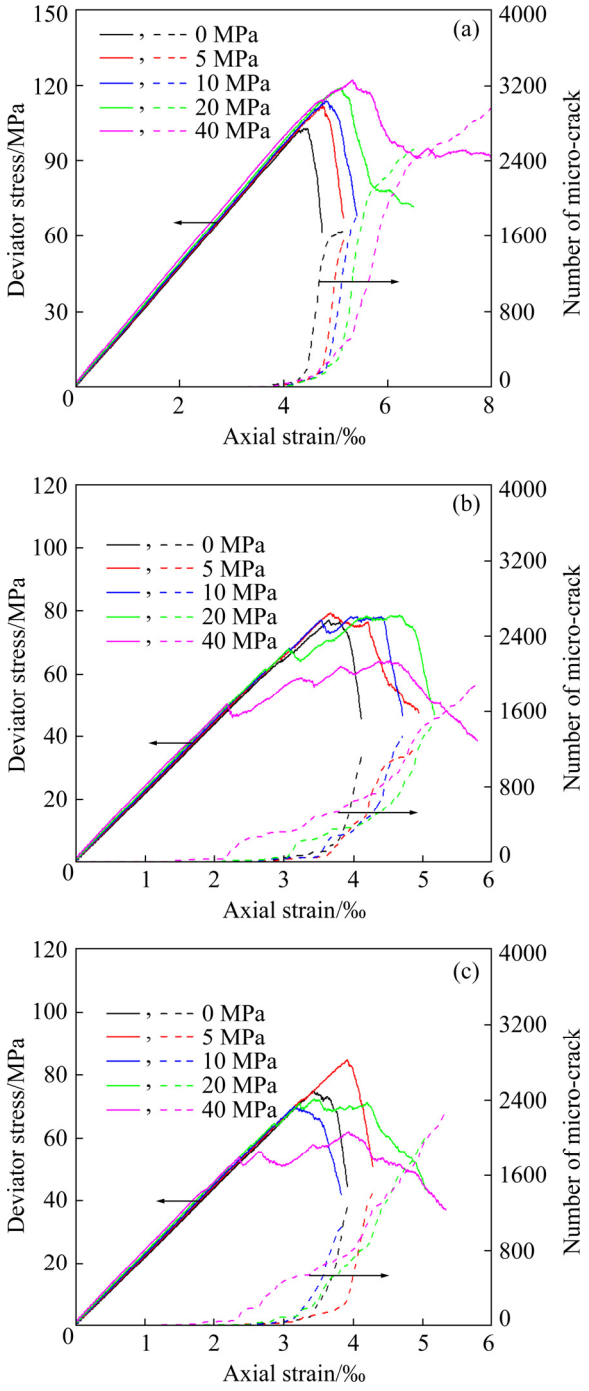


**Fig. 2** Curves of deviator stress and number of micro-crack versus axial strain subjected to different confining stresses: (a) Intact model; (b) Model containing circular opening; (c) Model containing horseshoe-shaped opening

the model with a circular opening is slightly larger than that of the model containing a horseshoe-shaped opening. From the above, we conclude that the excavated openings in rock weaken the mechanical properties appreciably, which is closely associated with the hole shape.

**Table 2** Mechanical parameters of models under different confining stresses

| Confining stress/MPa | Mechanical property | Intact model | Model with circular opening | Model with horseshoe-shaped opening |
|---|---|---|---|---|
| 0 | $\sigma_b$/MPa | 102.86 | 76.98 | 74.97 |
| | $E$/GPa | 22.02 | 19.75 | 19.78 |
| | $\varepsilon_p$/‰ | 4.44 | 3.65 | 3.43 |
| 5 | $\sigma_b$/MPa | 117.11 | 84.38 | 89.71 |
| | $E$/GPa | 22.44 | 20.94 | 20.91 |
| | $\varepsilon_p$/‰ | 4.75 | 3.67 | 3.92 |
| 10 | $\sigma_b$/MPa | 124.11 | 88.24 | 80.10 |
| | $E$/GPa | 22.77 | 21.34 | 21.36 |
| | $\varepsilon_p$/‰ | 4.83 | 4.05 | 3.15 |
| 20 | $\sigma_b$/MPa | 139.50 | 98.62 | 92.48 |
| | $E$/GPa | 23.27 | 21.89 | 21.90 |
| | $\varepsilon_p$/‰ | 5.10 | 4.66 | 3.44 |
| 40 | $\sigma_b$/MPa | 162.36 | 104.29 | 102.00 |
| | $E$/GPa | 23.99 | 22.87 | 22.78 |
| | $\varepsilon_p$/‰ | 5.33 | 4.52 | 3.94 |

### 2.3 Crack initiation, propagation and coalescence

By the PFC software, the mechanical responses of the above models under biaxial compression can be reproduced, and then the fracture behaviors were discussed. Taking uniaxial compression test as an example, the fracture morphologies of the pre-holed models at different time steps are presented in Fig. 3. In the figure, the numbers 1, 2, 3 and 4 represent the primary-tensile crack, sidewall crack, secondary-tensile crack and shear crack, respectively, while the lowercase in the upper-right corner of the number means the order in which the cracks occur.

For the model with a circular opening (see Fig. 3(a)), it is observed that two vertical primary-tensile cracks ($1^a$ and $1^b$) basically appear at the same time on the floor and roof of the circular opening, respectively. As the applied load increases, sidewall cracks $2^a$ and $2^b$ are observed to appear on both sides of the opening in sequence. During this period, three secondary-tensile cracks ($3^a$ to $3^c$) occur simultaneously on the three corners of the opening. The cracks are in parallel with the load

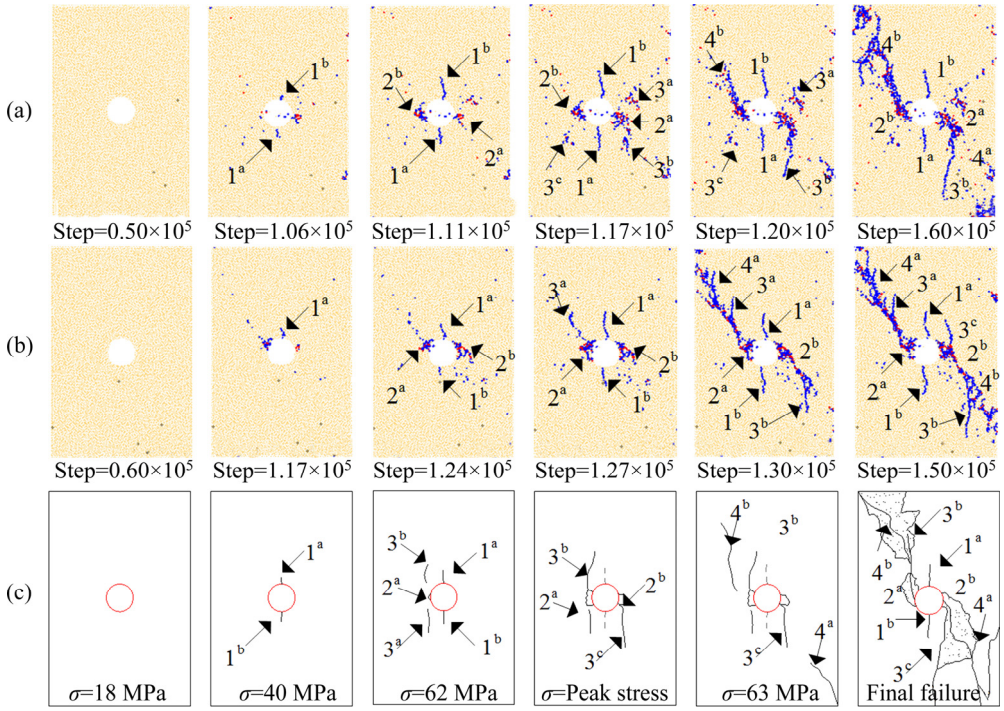


**Fig. 3** Crack evolution around openings under uniaxial compression: (a) Model with circular opening; (b) Model with horseshoe-shaped opening; (c) Real rock specimen containing circular hole [27]

orientation. Afterwards, two shear cracks $4^a$ and $4^b$ initiate from the lower-right and upper-left corners of the model, and propagate towards the opening sides until failure occurs. Clearly, the shear failure mode of the model is attributed to the coalescence of the shear cracks and sidewall cracks, while the tensile cracks do not play a critical role in the failure. On the whole, the fracture in the model under uniaxial compression evolves from primary-tensile cracks, sidewall cracks via secondary-tensile cracks and shear cracks, which is consistent with our previous experimental findings through DIC technique (see Fig. 3(c)) [27].

As illustrated in Fig. 3(b), the fracture response of the horseshoe-shaped opening subjected to uniaxial loads is also displayed clearly. At the beginning of the loading, no macro cracks are found since only elastic deformation occurs in the model. When the model enters plastic deformation stage, firstly, a primary-tensile crack $1^a$ along the loading direction is formed on the top of the opening. Subsequently, the other primary-tensile crack $1^b$ emerges on the floor. Meanwhile, plenty of sidewall cracks concentrate on the two sidewalls. After that, the secondary-tensile cracks and shear cracks appear in turn, which is similar to those of the circular opening. Finally, the shear-typed failure occurs due to the connection between the shear cracks and the sidewall cracks. In brief, there are also four types of cracks formed around the horseshoe-shaped opening. The main difference in crack evolution from the circular opening is that the two primary-tensile cracks do not occur simultaneously.

Figure 2 also presents the variation of number of micro-cracks during the loading process. It is found that few micro-cracks can be seen at the first deformation stage. When the plastic deformation stage is reached, the number of the micro-cracks increases due to the formation of macro-cracks. After the peak stress, a significant increase in the number of micro-cracks is found, which is caused by the coalescence of cracks. Moreover, the ultimate failure patterns of the models under different confining stresses are shown in Fig. 4. When the confining stress is applied, the lateral deformation is limited. Thus, the tensile cracks gradually disappear as the confining stress increases. Instead, more and more sidewall cracks and shear cracks appear, and the failure mode of the models is still shear failure. At this time, it is very likely to induce a violent rock burst. Also, it is found that the number of micro shear cracks is more and more with the increase of the confining stress.

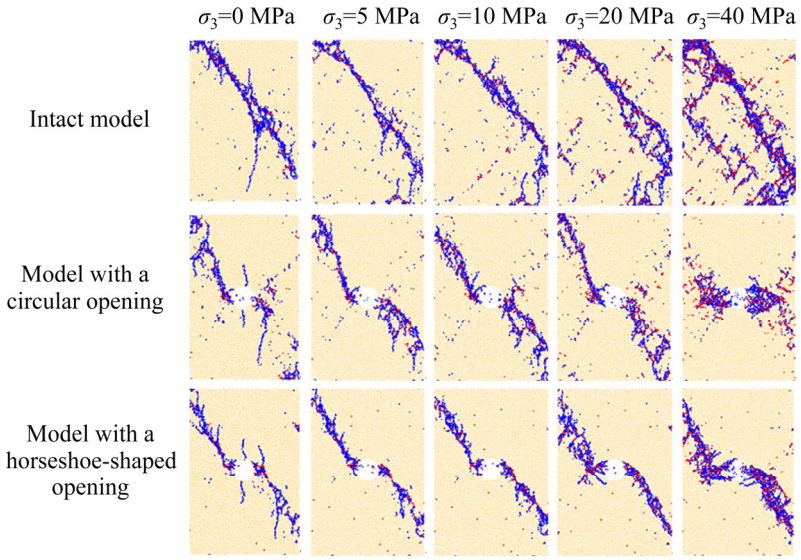


**Fig. 4** Failure modes of models under different confining stresses (The blue and red lines represent the tensile and shear micro-cracks, respectively)

## 3 Improved complex variable method of solving analytical stress solution

### 3.1 Complex variable theory

According to the plane strain hypothesis, a deep-buried tunnel in natural rock mass can be regarded as an infinite plate with a single hole. In the first place, the rock mass needs to be assumed as a homogeneous, continuous, and anisotropic elastic medium. Also, the stress gradient is ignored in this work. Thereby, the stress solution of the plane problem is ultimately equivalent to finding a biharmonic equation on the basis of a certain stress boundary, which can be expressed as

$$\frac{\partial^4 U}{\partial x^4}+2\frac{\partial^4 U}{\partial x^2\partial y^2}+\frac{\partial^4 U}{\partial y^4}=0 \tag{1}$$

where $U(x, y)$ means the Airy stress function of $x$ and $y$, which is a biharmonic function.

In accordance with the theory of elasticity, the general solution of Eq. (1) can be formulated as

$$\sigma_x=\frac{\partial^2 U}{\partial y^2}-f_x x,\quad \sigma_y=\frac{\partial^2 U}{\partial x^2}-f_y y,\quad \tau_{xy}=-\frac{\partial^2 U}{\partial x\partial y} \tag{2}$$

where $\sigma_x$, $\sigma_y$ and $\tau_{xy}$ are the normal stresses along $x$ and $y$ axes as well as their shear stress, while $f_x$ and $f_y$ represent the physical components along the $x$- and $y$-axis, respectively.

In general, semi-inverse method or inverse method is widely employed to solve these stress components. Nevertheless, under conditions of complex external forces or boundary, it is almost impossible to determine the form of the expression of the Airy stress function $U(x, y)$ or stress components ($\sigma_x$, $\sigma_y$ and $\tau_{xy}$). Complex variable methodology exhibits strong ability to deal with this issue. This is because the complex shaped boundaries can be transformed into simple shaped boundaries through conformal transformation. Afterwards, a set of procedural solutions that do not require trial and error can be used to solve the stress function. In 1898, Goursat first found the complex representation of the Airy stress function $U(z)$ ($z$=$x$ + i$y$, and $z$ is complex number) [28], namely,

$$U=\mathrm{Re}[\theta_1(z)+\overline{z}\varphi_1(z)] \tag{3}$$

where $\theta_1(z)$ and $\varphi_1(z)$ denote two analytical functions of the complex number $z$; $z$ and $\overline{z}$ are conjugate to each other; Re stands for the real part of a complex number.

As stated by MUSKHELISHVILI [29], introducing another analytical function $\psi_1(z)$ and letting $\psi_1(z)=\theta_1'(z)$, and then the complex forms of the three stress components can be written as follows:

$$\begin{cases}\sigma_x+\sigma_y=4\,\mathrm{Re}[\varphi_1'(z)]\\ \sigma_y-\sigma_x+2\mathrm{i}\tau_{xy}=2[\overline{z}\varphi_1''(z)+\psi_1'(z)]\end{cases} \tag{4}$$

In Eq. (4), the number of apostrophes in the

analytical function indicates the order of derivative. Moreover, the complex representation of the stress boundary condition is given as follows:

$$\varphi_1(z)+z\overline{\varphi_1'(z)}+\overline{\psi_1(z)}=\mathrm{i}\int_A^B(X+\mathrm{i}Y)\mathrm{d}s \tag{5}$$

where $A$ is the starting point of the integration taken on the boundary $s$, $B$ is an arbitrary point on the boundary, and $X$ and $Y$ are the surface force components along the $x$- and $y$-axis directions on the boundary, respectively. Providing that no support is applied to the tunnel boundary, the values of $X$ and $Y$ are both zero.

In regard to the simply connected domain problem in an infinite domain, the expressions of $\varphi_1(z)$ and $\psi_1(z)$ are defined as

$$\begin{cases}\varphi_1(z)=-\dfrac{1}{2\pi(1+\kappa)}(X+\mathrm{i}Y)\ln z+Bw(z)+\varphi_1^0(z)\\ \psi_1(z)=\dfrac{\kappa}{2\pi(1+\kappa)}(X-\mathrm{i}Y)\ln z+\\ \qquad (B'+\mathrm{i}C')w(z)+\psi_1^0(z)\end{cases} \tag{6}$$

where $\kappa$ means a real number coefficient which can be calculated by $(3-\mu)/(1+\mu)$ in this work; $\mu$ is the Poisson's ratio of the rock; $B$, $B'$ and $C'$ are three real constants, which are expressed by

$$B=\left(\sigma_x^\infty+\sigma_y^\infty\right)/4,\quad B'=\left(\sigma_y^\infty-\sigma_x^\infty\right)/2,\quad C=\tau_{xy}^\infty \tag{7}$$

where $\sigma_x^\infty$, $\sigma_y^\infty$ and $\tau_{xy}$ denote the components of the applied stress filed to the boundary of the infinite plate (see Fig. 5).

In Eq. (6), $\varphi_1^0(z)$ and $\psi_1^0(z)$ represent two single valued holomorphic functions within the neighborhood of infinity, and their formulae can be expanded into Laurent series yields:

$$\varphi_1^0(z)=\sum_{n=1}^{\infty}a_nz^{-n},\ \psi_1^0(z)=\sum_{n=1}^{\infty}b_nz^{-n} \tag{8}$$

where $a_n$ and $b_n$ are real constants provided that there is no external force acting on the tunnel boundary. Otherwise, they are complex constants.

### 3.2 Conformal transformation

Riemann mapping theorem shows that there must be a mapping function that can transform the complex boundary of a simply connected domain in the physical plane $z$ to a unit circle in the image plane $\zeta$. In this way, the analytical stress solution of the complex shaped hole can be easily solved although the form of its stress boundary after mapping becomes complicated. Apparently, any point or line in the $z$-plane has a mapped point or mapped line in the $\zeta$-plane corresponding to it. Likewise, this also works for plane figure. It is noticeable that the shape of the figure may rotate and stretch after the mapping, but the angle between any two intersecting curves remains the same. Hence, this mapping is also called conformal transformation (Fig. 5).

In this work, the outer region of the horseshoe-shaped tunnel in the $z$-plane was mapped to the outer region of the unit circle in the $z$-plane via conformal transformation. Figure 5 also illustrates the in-situ stress field applied around the infinite plate, that is, $\sigma_x^\infty=p$, $\sigma_y^\infty=\lambda p$ ($\lambda$ denotes lateral stress coefficient) and $\tau_{xy}^\infty=0$. The sign convention for stress is specified as follows: positive values and negative values mean tensile stresses and compressive stresses, respectively. Assuming the expression of the mapping function is $z=w(\zeta)$ ($\zeta=\xi+i\eta$), then by substituting it into Eqs. (4), (7) and (8), we have

$$\begin{cases}\sigma_\rho+\sigma_\theta=4\mathrm{Re}[\Phi(\zeta)]\\ \sigma_\theta-\sigma_\rho+2\mathrm{i}\tau_{\rho\theta}=\dfrac{2\zeta^2}{\rho^2w'(\zeta)}\cdot\\ \qquad[\overline{w(\zeta)}\Phi'(\zeta)+w'(\zeta)\Psi(\zeta)]\end{cases} \tag{9}$$

where $\sigma_\rho$, $\sigma_\theta$ and $\tau_{\rho\theta}$ denote three stress components of a point $z=(r, a)$ in polar form; $\rho$ and $\theta$ represent the polar radius and polar angle of its mapping point, respectively; $w'(\zeta)$ and $\Phi'(\zeta)$ are the first derivatives of the original functions $w(\zeta)$ and $\Phi(\zeta)$, respectively. $\overline{w(\zeta)}$ and $w(\zeta)$ are conjugated to each other.

The formulae of the complex potential functions $\Psi(\zeta)$ and $\Phi(\zeta)$ in Eq. (9) can be obtained by

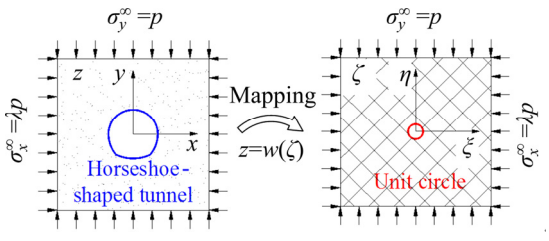


**Fig. 5** Schematic of conformal transformation

$$\Phi(\zeta)=\varphi_1'(z)=\frac{\varphi'(\zeta)}{w'(\zeta)},\quad \Psi(\zeta)=\psi_1'(z)=\frac{\psi'(\zeta)}{w'(\zeta)} \tag{10}$$

Furthermore, by replacing $z$ with $\zeta$, the equation of stress boundary condition is simplified as

$$\varphi_0(\sigma)+\frac{w(\sigma)}{\overline{w'(\sigma)}}\overline{\varphi_0'(\sigma)}+\overline{\psi_0(\sigma)}= f(\sigma)-2Bw(\sigma)-(B'-\mathrm{i}C')\overline{w(\sigma)} \tag{11}$$

where $\sigma$ denotes the point located on the boundary of the unit circle, namely, $\zeta=\sigma$. It is emphasized that the influence of tunnel support on the surrounding stress distribution is ignored in this work, i.e., no external force acts on the tunnel boundary so that both the values of $X$ and $Y$ are zero. Thus, $f(\sigma)=\int_A^B(X_n+\mathrm{i}Y_n)\mathrm{d}s$ is also equal to zero.

From the description above, it is concluded that we need to solve the mapping function $z=w(\zeta)$ first, and then substitute it into Eq. (11) combined with Eqs. (6), (7), (8) and (10). As a result, the values of all the unknown numbers $a_n$ and $b_n$ in Eq. (8) can be found using power series method. Afterwards, the expressions of the complex potential functions $\Psi(\zeta)$ and $\Phi(\zeta)$ can be derived. Moreover, by substituting them further into Eq. (9) and solving the system of equations, it is easy to acquire the formulae of the three stress components ($\sigma_\rho$, $\sigma_\theta$ and $\tau_{\rho\theta}$) by MATLAB code.

### 3.3 Solution of mapping function

Since only the analytical function possesses the property of conformal transformation, the mapping function must be an analytical function. Generally, the expression of the mapping function can be expanded into a form of Laurent series, namely,

$$z=\omega(\zeta)=K(\zeta+\sum_{m=0}^{\infty}C_m\zeta^{-m})\ \ (\|\zeta\|\geq 1) \tag{12}$$

where $K$ is a real-valued number associated with the cross-sectional shape of tunnel; $C_m$ ($m$ is a positive integer from zero to infinity) is a real-valued constant if the tunnel cross section has more than one axis of symmetry, otherwise it is a complex-valued constant.

As shown in Eq. (12), the number of terms of the expression is infinite. Obviously, it is impossible to find the strict solution of the mapping function. However, literature [30] demonstrates that the mapping effect is good enough when a few terms of $C_m$ for mapping function are taken.

Supposing the coordinates of a point $A_j$ on the tunnel boundary in the $z$-plane were ($r_j$, $a_j$) and those of its mapping point $B_j$ in the $\zeta$-plane were (1, $\theta_j$), then the two points can be written in polar coordinate forms as

$$z=r_j\mathrm{e}^{\mathrm{i}\alpha_j},\quad \zeta=\mathrm{e}^{\mathrm{i}\theta_j} \tag{13}$$

Introducing Eq. (13) into Eq. (12), and then expanding the expressions on the two sides of the equation in light of Euler's formula, we get

$$r_j(\cos\alpha_j+\mathrm{i}\sin\alpha_j)=K\left(\cos\theta_j+\mathrm{i}\sin\theta_j+\sum_{m=0}^{\infty}C_m[\cos(m\theta_j)-\mathrm{i}\sin(m\theta_j)]\right) \tag{14}$$

Decomposing the expressions on both sides of Eq. (14) into two parts of real and imaginary, leads to

$$\begin{cases}\sin(\alpha_j-\theta_j)+\sum_{m=0}^{\infty}C_m\sin(\alpha_j+m\theta_j)=0\\ r_j=K[\cos(\alpha_j-\theta_j)+\sum_{k=0}^{\infty}C_m\cos(\alpha_j+m\theta_j)]\end{cases} \tag{15}$$

By substituting the coordinates ($r_j$, $a_j$) ($j$=1, 2, 3, ⋯) of a large number of sampling points on the tunnel boundary into Eq. (15), the values of variables $C_m$, $K$ and $\theta_j$ can be obtained by solving a system of equations. In this work, the dimensions of the selected tunnel are about 1.5 times those of the headrace tunnel 4# of the Jinping II Hydropower Station (see Section 5), but their shapes are exactly the same. As the tunnel shape has an axis of symmetry, we take the left half of the tunnel boundary as the research object, and divide it evenly into 30 parts. Consequently, a total of 31 sampling points is formed, which are named counterclockwise from $A_1$ to $A_{31}$, respectively. Accordingly, their mapping points on the unit circle are named from $B_1$ to $B_{31}$, respectively. Besides, the coordinate systems in $z$-plane and $\zeta$-plane are both rotated by 90°, as illustrated in Fig. 6. For the first and last points ($A_1$ and $A_{31}$) on the tunnel boundary, the locations of their mapping points ($B_1$ and $B_{31}$) on the unit circle are consistent, i.e., $B_1$=(1, 0) and $B_{31}$=(1, π). Thus, assuming $n$ terms of $C_m$ are considered, the relation between $C_m$ and $K$ can be obtained by substituting the coordinates of $A_1$ and $B_1$ into Eq. (15), namely,

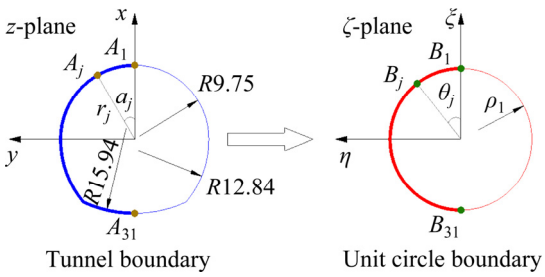


**Fig. 6** Schematic diagram of sampling points and mapping points

$$K = r_1 \Big/ \left(1 + \sum_{m=0}^{n-1} C_m\right) \tag{16}$$

Apparently, the first identity in Eq. (15) is not valid if finite terms of $C_m$ are taken into account. Therefore, the solution of the mapping function in such a case is equivalent to optimizing a constrained object function as follows:

$$\begin{aligned} &\min f(C_m, \theta_j, r_1) = \sum_{j=1}^{31} \left\{ r_j - r_1 \left[ \cos(\alpha_j - \theta_j) + \right.\right. \\ &\left.\left. \sum_{m=0}^{n-1} C_m \cos(\alpha_j + m\theta_j) \right] \Big/ \left(1 + \sum_{m=0}^{n-1} C_m\right) \right\}^2 \\ &\text{s.t. } \sin(\alpha_j - \theta_j) + \sum_{m=0}^{n-1} C_m \sin(\alpha_j + m\theta_j) = 0 \quad (\text{I}) \\ &\sum_{m=0}^{n-1} m|C_m| < 1 \quad (\text{II}) \end{aligned} \tag{17}$$

In this research, a shrinkage approximation algorithm was proposed to optimize the above function. The principle of the method is: by repeatedly calculating and comparing the function value of each vertex of the polyhedron, finding the vertex with the largest function value and replacing it with a new vertex. When the vertex that meets the requirements appears, stop the iteration. Detailed calculation procedures are described as follows.

Step 1: Assume that the selected number of $C_m$ was $n$, a primary polyhedron with $k_d$ ($k_d$=$n$+1 in this study) vertices in $n$-dimensional space needs to be constructed firstly. Each vertex represents a group of possible solution. The vector of the first vertex is defined as (0, 0, 0, ⋯, 0), while the element values of the other ($k_d$ −1) vertices are randomly assigned using the following equation:

$$\begin{aligned} &x_i^j = a_i + \eta_i^j (b_i - a_i) \\ &(i = 1, 2, \cdots, n;\ j = 2, 3, \cdots, k_d) \end{aligned} \tag{18}$$

where $x_i^j$ denotes the value of element; $a_i$ and $b_i$ represent the maximum and minimum values of $C_m$, respectively; $\eta_i^j$ means a random coefficient with a value range of [0, 1].

Afterwards, check whether the element values of all vertices of the primary polyhedron meet the constraint II. If not, re-assign the element values of the vertices according to Eq. (18); otherwise, proceed to the next step.

Step 2: Calculate the function values $f(X^j)$ of all vertices, and find the "good" vertex $X^j_{\min}$ whose function value $f(X^j_{\min})$ is the smallest, the "bad" vertex $X^j_{\max}$ with the largest function value ($f(X^j_{\max})$), and the "secondary-bad" vertex $X^j_{\max 2}$ whose function value $f(X^j_{\max 2})$ is the second largest.

Step 3: Determine if the convergence conditions are met, according to

$$\left\{ \frac{1}{k_d - 1} \sum_{j=1}^{k_d - 1} \left[ f(X^j) - f(X^j_{\min}) \right]^2 \right\}^{0.5} \le \delta \tag{19}$$

where $\delta$ denotes the admissible error, and the value is set to $10^{-6}$ in this research.

Substitute the function values of all the vertices into Eq. (19) to see whether it holds. If it is satisfied, stop the iteration, and the vertex $X^j_{\min}$ with the smallest function value $f(X^j_{\min})$ is the optimal solution. Otherwise, move on to the following step.

Step 4: Find the centroid $X^C$ of all the vertices except the "bad" vertex $X^j_{\max}$, and check if it satisfies the constraint II. If yes, go to the next step. If not, return to step 1 to generate a new primary polyhedron (whose centroid is thus written as $X^{C1}$) by replacing $a_i$ and $b_i$ with $X^j_{\min}$ and $X^C$, respectively, until all the vertices of the new primary polyhedron satisfy the constraint II.

Step 5: Find the reflection point $X^{R1}_{\max}$ of the "bad" vertex $X^j_{\max}$ along the line connecting the centroid $X^C$ and the 'bad' vertex $X^{R1}_{\max}$ by

$$X^{R1}_{\max} = X^C + \chi\left(X^C - X^j_{\max}\right) \tag{20}$$

where $\chi$ is the reflection coefficient, whose initial value is determined as 1.3.

Next, verify whether the reflection point $X^{R1}_{\max}$ meets the constraint II and the function values of the reflection point $X^{R1}_{\max}$ is less than that of the "bad" vertex $X^j_{\max}$. If yes, jump to the next step; otherwise, halve the reflection coefficient $\chi$ in Eq. (20) to regenerate a new reflection point. If the

reflection coefficient $\chi$ is continuously reduced to $1\times10^{-8}$ and no satisfactory reflection point is found, we need to neglect the "bad" vertex $X^{j}_{\max}$ and keep finding the reflection point $X^{R2}_{\max}$ of the "secondary-bad" vertex $X^{j}_{\max2}$ based on steps 4 and 5. Repeat this step until a satisfactory reflection point $X^{Rk}_{\max}$ is generated, as presented in Fig. 7.

Step 6: Replace the "bad" vertex $X^{j}_{\max}$ with the reflection point $X^{Rk}_{\max}$, and go back to Step 2.

The above procedures are implemented through a written MATLAB code. For different numbers of $C_m$, the optimization results of $C_m$, $K$ and the corresponding function values are listed in Table 3.

To conclude, the objective function value decreases as the number of $C_m$ increases. It can be seen that the value of the objective function is already very close to zero when the number of $C_m$ is 8. Thus, substituting the values of $C_m$ in such a case into Eq. (12), and then the mapping function of the horseshoe-shaped tunnel can be obtained as

$$z=w(\zeta)=6.61\zeta-0.16+\frac{0.02}{\zeta}+\frac{0.10}{\zeta^2}-\frac{0.13}{\zeta^3}+\frac{0.08}{\zeta^4}-\frac{0.03}{\zeta^5}-\frac{0.01}{\zeta^6}+\frac{0.03}{\zeta^7} \tag{21}$$

Figure 8 illustrates the mapped tunnel shapes under the condition of different terms of mapping function. It is found that the mapped tunnel shape and the actual shape basically coincide under the condition that the number of $C_m$ terms is 8. This fully proves that the proposed shrinkage approximation method for solving the mapping function is efficient and reliable.

### 3.4 Stress distribution around tunnel

In light of Eq. (20), the following transformation of the mapping function can be found:

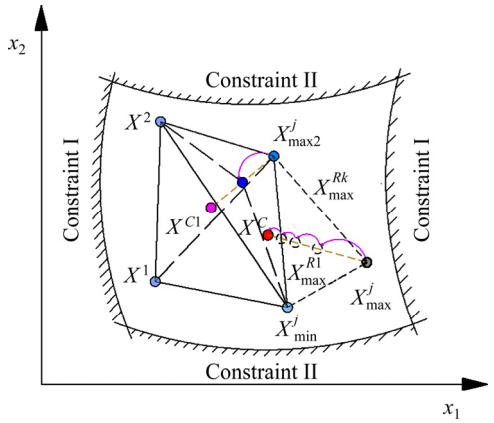


**Fig. 7** Schematic diagram for determining reflection point

$$w(\sigma)=6.61\sigma-0.16+0.02\sigma^{-1}+0.10\sigma^{-2}-0.13\sigma^{-3}+0.08\sigma^{-4}-0.03\sigma^{-5}-0.01\sigma^{-6}+0.03\sigma^{-7} \tag{22}$$

$$\overline{w(\sigma)}=6.61\sigma^{-1}-0.16+0.02\sigma+0.10\sigma^{2}-0.13\sigma^{3}+0.08\sigma^{4}-0.03\sigma^{5}-0.01\sigma^{6}+0.03\sigma^{7} \tag{23}$$

$$\overline{w'(\sigma)}=6.61-0.02\sigma^{2}-0.19\sigma^{3}+0.40\sigma^{4}-0.32\sigma^{5}+0.14\sigma^{6}+0.07\sigma^{7}-0.20\sigma^{7} \tag{24}$$

where $\sigma$ stands for the point on the unit circle boundary, i.e., $\zeta=\sigma$.

Combining Eq. (8), substituting Eqs. (22)−(24) into Eq. (11), and then the values of $a_n$ and $b_n$ can be solved by power series method. However, we found that the term number of $a_n$ is seven, but that of $b_n$ is infinite. As the value of $n$ increases, it is seen that the value of $b_n$ gradually approaches to zero. For example, $b_{98}=(1.06\times10^{-15}-1.86\times10^{-14}\lambda)p$, $b_{99}=(-9.77\times10^{-15}+1.40\times10^{-14}\lambda)p$ and $b_{100}=(9.69\times10^{-15}-5.12\times10^{-15}\lambda)p$. In this work, the term number of $b_n$ is determined as 100. This simplified treatment has little effect on the stress results. Therefore, the expressions of $\varphi_1(\zeta)$ and $\psi_1(\zeta)$ can be derived according to Eqs. (6)−(8), which are shown as follows:

**Table 3** Optimization results of $C_m$, $K$, and function values using shrinkage approximation method

| Number of $C_m$ | Function value | $K$ | $C_0$ | $C_1$ | $C_2$ | $C_3$ | $C_4$ | $C_5$ | $C_6$ | $C_7$ |
|---|---|---|---|---|---|---|---|---|---|---|
| 3 | 0.4854 | 6.6003 | −0.0269 | −0.0014 | 0.0131 | − | − | − | − | − |
| 4 | 0.1781 | 6.6198 | −0.0219 | 0.0043 | 0.0178 | −0.0183 | − | − | − | − |
| 5 | 0.0403 | 6.6124 | −0.0257 | 0.0023 | 0.0144 | −0.0204 | 0.0124 | − | − | − |
| 6 | 0.0260 | 6.6138 | −0.0249 | 0.0031 | 0.0148 | −0.0195 | 0.0132 | −0.0039 | − | − |
| 7 | 0.0252 | 6.6144 | −0.0247 | 0.0034 | 0.0150 | −0.0191 | 0.0130 | −0.0036 | −0.0013 | − |
| 8 | 0.0188 | 6.6131 | −0.0249 | 0.0025 | 0.0146 | −0.0200 | 0.0122 | −0.0042 | −0.0017 | 0.0044 |

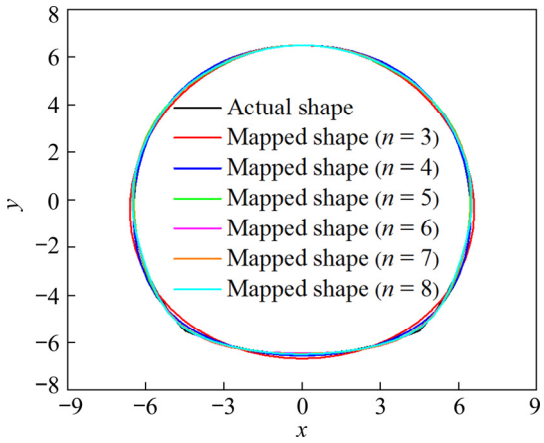


**Fig. 8** Comparison of actual tunnel shape and mapped ones

$$\begin{cases}\varphi_1(\zeta)=p[0.04(\lambda+1)p+1.65(\lambda+1)p\zeta+\dfrac{(3.24-3.25\lambda)p}{\zeta}+\dfrac{(0.01-0.06\lambda)p}{\zeta^2}+\dfrac{(0.02+0.05\lambda)p}{\zeta^3}-\dfrac{(0.03+0.02\lambda)p}{\zeta^4}+\dfrac{(0.02\lambda-0.02)p}{\zeta^5}-\dfrac{0.01(\lambda+1)p}{\zeta^7}]\\ \psi_1(\zeta)=-p[-0.08(\lambda-1)p+3.31(\lambda-1)p\zeta-\dfrac{(3.30+3.33\lambda)p}{\zeta}+\dfrac{(-0.08+0.09\lambda)p}{\zeta^2}+\dfrac{(3.24-3.26\lambda)p}{\zeta^3}+\cdots+\dfrac{p(9.69\times10^{-15}-5.12\times10^{-15}\lambda)}{\zeta^{100}}]\end{cases} \quad (25)$$

Substituting Eq. (25) into Eqs. (10) and (9), and then the three stress components ($\sigma_\rho$, $\sigma_\theta$ and $\tau_{\rho\theta}$) at any point in the surrounding rock of the tunnel can be obtained by solving the equation system. On the boundary of the horseshoe-shaped tunnel, the tangential stress distributions at different lateral stress coefficients are shown in Fig. 9. Since there is no load or support on the perimeter of the tunnel, the radial stress and shear stress are both zero regardless of the lateral stress coefficient.

As can be seen in Fig. 9, the hoop stress distribution on the boundary of the tunnel varies with the lateral stress coefficient significantly. When $\lambda$ is 0, the maximum tensile stresses formed on the roof and floor of the tunnel are $-1.0p$ and $-0.95p$. In contrast, the two sidewalls of the tunnel

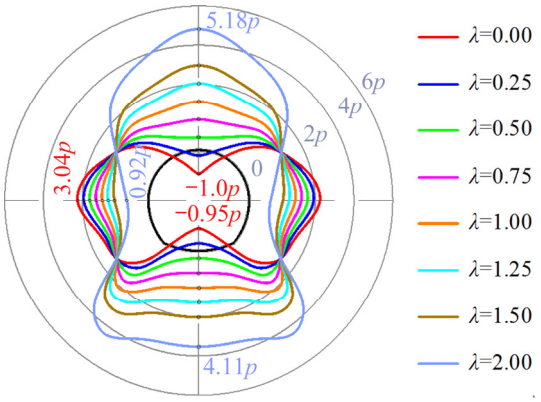


**Fig. 9** Tangential stress distribution on tunnel boundary under different lateral stress coefficients

are concentrated by compressive stress, with a maximum value of $3.04p$. As the lateral stress coefficient increases, both the tensile and compressive stresses decrease. When $\lambda$ increases to about 0.327, the tensile stress on the top disappears, while the maximum tensile stress on the bottom reduces to $-0.12p$. At this time, the maximum compressive stress appearing on the sidewalls is $2.69p$. With the continuous rise of the lateral stress coefficient, it is found that, when $\lambda$ reaches 0.375, the tensile stress on the floor begins to turn to compressive stress. At this moment, the maximum stresses on the two sides of the tunnel are $2.64p$, while that on the roof is $0.15p$. After that, the stresses on the top and bottom of the tunnel grow with the increasing lateral stress coefficient, while the compressive stress concentrated on the two sides declines gradually. With the increase of lateral stress coefficient to 2, it is found that the stress concentration factors on the roof, floor and sidewalls are 5.18, 4.11 and 0.92, respectively. Moreover, we further calculated that, when $\lambda$=3, the stress concentration factors at the centers of the roof, floor and sidewall are 8.28, 6.64 and −0.13, respectively, whereas those are 11.38, 9.17 and −1.19, respectively, under $\lambda$=4. To sum up, as the lateral stress coefficient rises, the stresses on the top and bottom of the tunnel change from tensile stress to increasing compressive stress, while the opposite situation occurs on the side walls. The hoop stress distribution on the perimeter of the tunnel is remarkably related to the in-situ stress, particularly the lateral stress coefficient.

Additionally, the radial and hoop stresses of any point away from the tunnel boundary can also

be calculated. Figure 10 shows the stress distributions at distances of one, three and five times the polar radius from the tunnel boundary. Since the tunnel shape has an axis of symmetry (see Fig. 6), the surrounding stress distribution must be symmetrical about it.

As shown in Fig. 10, for hoop stress distribution, the stress concentration factor decreases with the increase of the distance from the tunnel boundary. When $\lambda$ is 0, the maximum hoop stress on the top location of the tunnel drops from 0.03$p$ at a distance of one time the polar radius to 0.01$p$ at a distance of three times the polar radius, while the change on the bottom location is the same. By contrast, the maximum stress concentration factor on the sides decreases from 1.23 to 1.02. As the lateral stress coefficient rises to 1, the compressive stress on the top turns from 1.26$p$ at $r$=2$r_1$ to 1.03$p$ at $r$=6$r_1$, whereas that on the bottom changes from 1.27$p$ at $r$=2$r_{31}$ to 1.03$p$ at $r$=6$r_{31}$. By comparison, the compressive stress concentration factor at the centers of sides reduces from 1.26 to 1.03. When the lateral stress coefficient approaches to 2, the stress evolution law with the increasing distance from the tunnel boundary is the same. That is to say, as the distance from the tunnel boundary

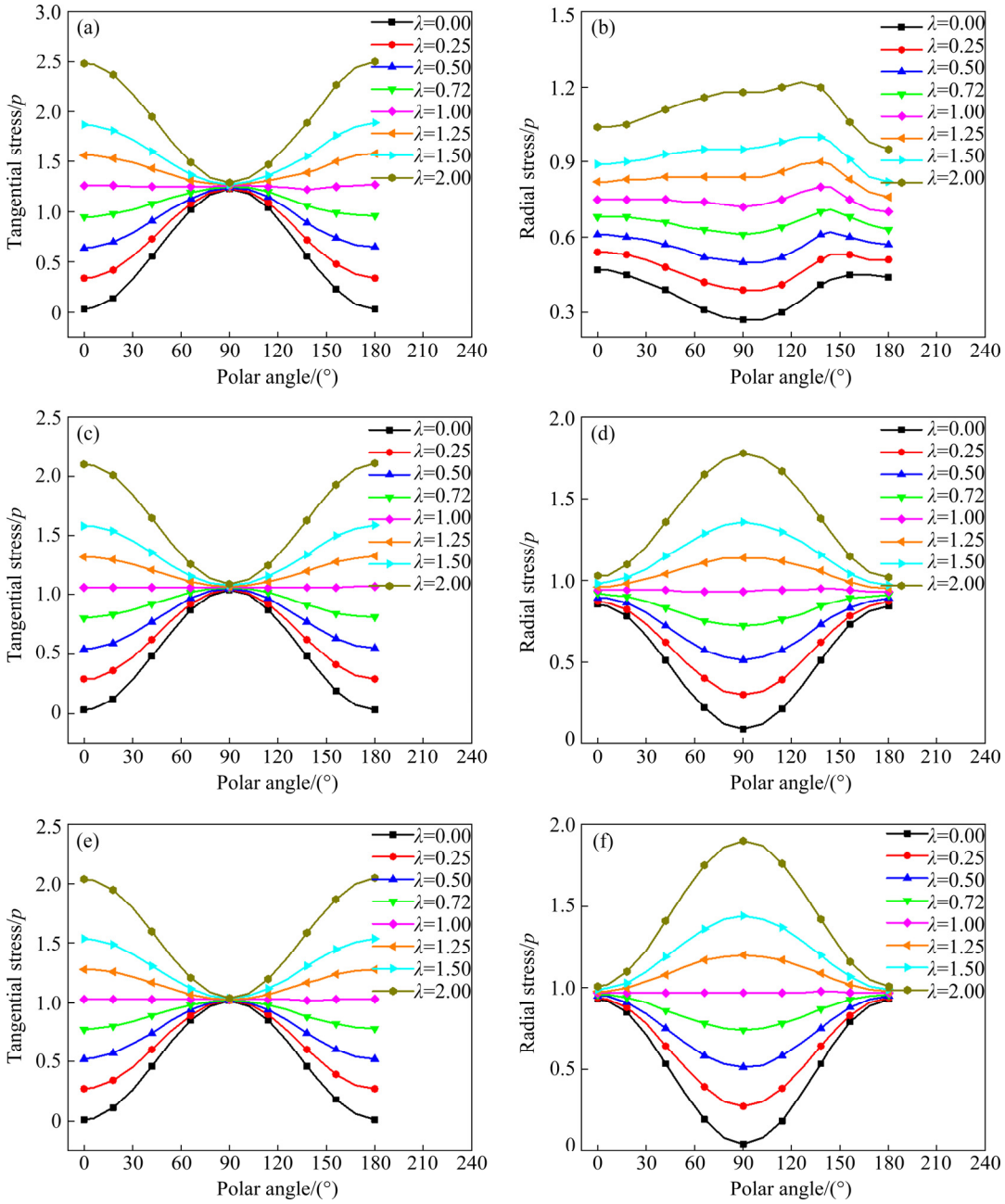


**Fig. 10** Tangential and radial stress distribution at different distances from tunnel boundary: (a, b) One times polar radius; (c, d) Three times polar radius; (e, f) Five times polar radius

grows, the maximum tangential stress on the roof and floor gradually decreases towards the horizontally applied stress, while that on the two sides progressively falls to the vertically acted stress.

Similarly, the radial stress distribution at the periphery of the tunnel can also be obtained utilizing this method. As the distance from the tunnel boundary increases, it is found that the radial stress on centers of the roof and bottom changes approximately to the applied vertical stress ($\sigma_x^{\infty}$), whereas that on the two sides changes gradually to the exerted horizontal stress ($\sigma_y^{\infty}$). For instance, when $\lambda$ is zero, the maximum radial stress on the roof increases from 0.47$p$ at $r$=2$r_1$ to 0.93$p$ at $r$=6$r_1$, while that on the tunnel side decreases from 0.27$p$ at $r$=2$r_{16}$ to 0.04$p$ at $r$=6$r_{16}$, Under the condition that $\lambda$ = 2, the maximum radial stress on the top and floor decreases from 1.04$p$ and 0.95$p$ at $r$=2$r_1$ to 1.01$p$ at $r$=6$r_1$, while that on the side rises from 1.18$p$ at $r$=2$r_{16}$ to 1.90$p$ at $r$=6$r_{16}$. In summary, the influence scope of the excavated tunnel on the stress distribution is about five times the tunnel dimension.

### 3.5 Reliability verification of proposed method

To verify the reliability of the complex variable method for solving the excavation-induced stress around the tunnel, a numerical investigation was further carried out using a finite element method. As the presented problem belongs to plane strain problem, the length, width and height of the model were set to 150, 0.5, and 150 m, respectively, which are more than ten times the maximum dimension of the tunnel (see Fig. 11(a)). Thus, the boundary effect can be neglected. Note that the dimensions of the tunnel to be excavated in the model were the same as that in Fig. 6. With regard to the mesh size of the model, it was divided in a non-uniform manner; that is, the mesh size of the zone near the tunnel was 0.05 m, while that away from the tunnel was 5 m. In this work, the body force was ignored and only the elastic stress state was considered. Thus, the elastic constitutive model was used to characterize the relation between stress and strain. According to the elastic mechanics theory, the inherent properties of material have no effect on the elastic stress distribution if the body force is constant. Consequently, the elastic modulus was defined to be large enough to shun the plastic deformation of the model. Besides, the six surfaces of the model were fixed along their normal direction.

During the modelling, to record the excavation-induced stress at different locations around the tunnel, three stress monitoring lines ($A$, $B$, $C$) were arranged on the top, bottom and left side of the tunnel, respectively. As shown in Fig. 11(b), each line contains 10 monitoring points with a spacing of 1.3 m. To facilitate calculation and comparative analysis, only a uniform stress of 20 MPa was applied to the upper and lower surfaces, i.e., $\sigma_x^{\infty}$=20 MPa and $\lambda$=0. In such a case, the monitored stresses of these monitoring points after the excavation of the tunnel were compared with the analytical results obtained by the proposed method, as shown in Fig. 12. The results indicate that the two methods show good agreement, and the average relative error of stress is only 0.29 MPa. The slight error of the numerical method results from the large size of the element. Actually, the monitored stress is owned by the barycenter of the element in which the monitor point is situated. Thus, the smaller the element dimension, the closer

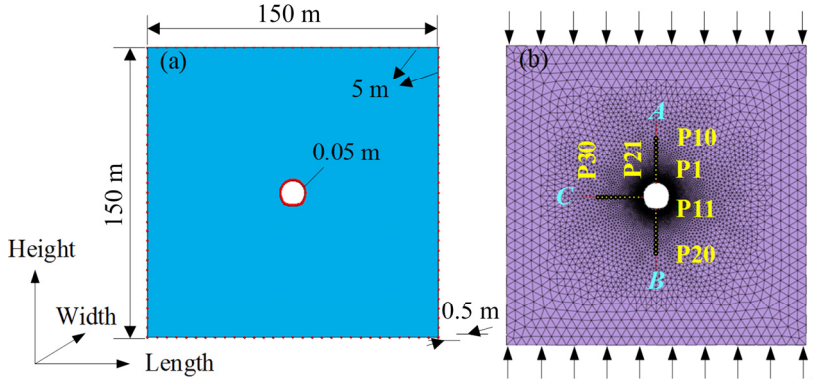


**Fig. 11** Numerical modelling: (a) Schematic of model size; (b) Location of stress monitoring point

the centroid of the element is to the monitoring point. However, this will lead to a great many elements and nodes, bringing difficulties for the computer to run. Overall, the proposed method for solving the analytical stress solution of the horseshoe-shaped tunnel is effective and reliable.

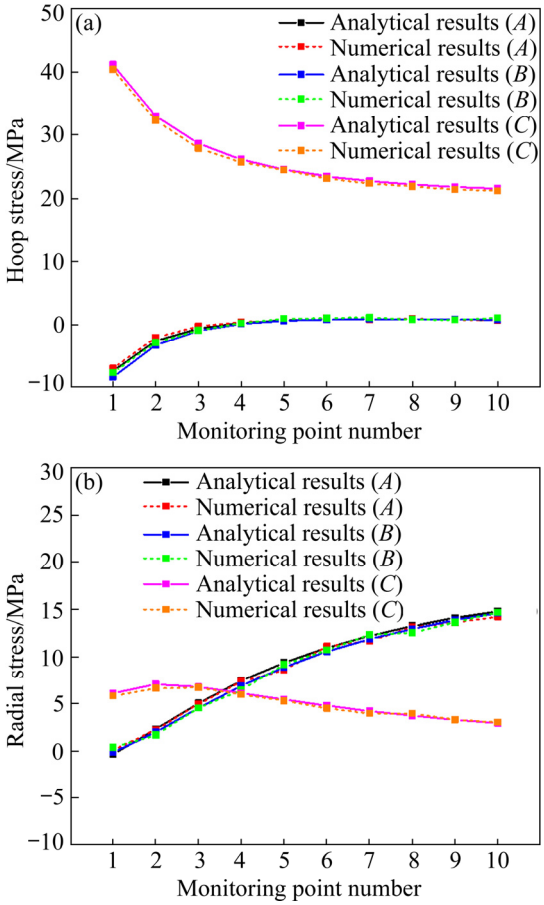


**Fig. 12** Comparison of analytical and numerical results of stress monitoring points: (a) Hoop stress; (b) Radial stress

## 4 Discussion on fracture mechanism

Actually, the fracture mechanism can be revealed according to the stress state in the model under loads. For the intact model, the stress states of the upper and lower ends under uniaxial compression are three-dimensional because of the end friction effect. As a result, a shear plane is formed along the major diagonal, and the final shear failure mode appears. As the confining stress increases, the splitting tensile cracks are inhibited. Thus, the failure is shear-dominated. With regard to the circular opening, the stress components at an arbitrary point around the opening can be solved using Kirsch equation, and the hoop stress distributions under different lateral stress coefficients on the hole boundary are illustrated in Fig. 13. Clearly, the tensile stresses occurring on the top and bottom of the opening lead to the formation of primary-tensile cracks (see Fig. 13). As the two stress values are equal, they initiate at the same time. Likewise, as the distance from the hole boundary rises, the tensile stress in the roof directly above the tunnel drops to zero, and then becomes compressive stress until it is equal to the exerted horizontal stress. Consequently, the primary-tensile cracks cease propagation when approaching a certain length. Next, the critical stress zone is transferred from the primary-tensile crack tip to the regions on its both sides. This gives rise to the occurrence of the secondary-tensile cracks. Meanwhile, due to the high level of concentrated compressive stress, the sidewall cracks gradually appear on the sidewalls. Generally, the secondary-tensile cracks develop towards the spalling zones until coalescence appears. When the exerted axial stress reaches a certain level, the shear cracks are induced by strong end friction effects and progressively propagate from the model corner to the spalling zones along the diagonal. Thus, the shear failure is formed eventually. With the growing of the confining stress, the formed tensile stress on the roof and floor disappears gradually. Instead, only compressive stress occurs around the opening. As the biaxial compressive strength is more than 2.5 times that of the confining stresses set in this study, the lateral stress coefficients are less than 0.5. Therefore, the maximum compressive stress is formed on the sidewalls rather than the top or the bottom. This is why spalling failure is getting worse on the sidewalls as the confining stress increases.

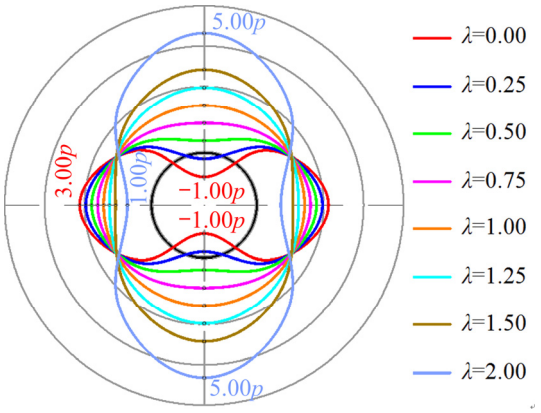


**Fig. 13** Hoop stress distribution on boundary of circular opening

In respect of the horseshoe-shaped opening, the fracture mechanism is similar to that of the circular opening. The reason why the primary-tensile crack on the roof under uniaxial compression initiates earlier than that on the floor is that the tensile stress concentration factor on the top location (−1.01) is larger than that on the bottom location (−0.95). Besides, we found that the stress concentration factors on the boundary of the circular opening are lower than those of the horseshoe-shaped opening at the same lateral stress coefficient. That is to say, the primary-tensile crack initiation stress of the circular opening is relatively large, and the spalling failure or rock burst is less serious. Therefore, the stability of the circular tunnel is higher than that of the horseshoe-shaped tunnel.

## 5 Case study of headrace tunnel of Jinping II Hydropower Station

### 5.1 Project overview

Jinping II Hydropower Station, the 9th largest hydropower station in the world, possesses a total installed capacity of 4.8 million kW and an average annual power generation of about 25 billion kW·h. It is situated on the Ya-lung River in Liangshan Yi autonomous Prefecture, Sichuan province, China. The Ya-lung River flows around Jinping Mountain, leading to a maximum water level difference of 308 m between the east and west sides. In the hydropower station, four parallel headrace tunnels (1#, 2#, 3# and 4#) through the mountain have been excavated for diverting water. Additionally, three other tunnels have also been constructed, including two auxiliary tunnels (A# and B#) for geological exploration and transportation and one drainage tunnel (C#) for discharging excess water, and the details can be found in Ref. [31]. From east to west, the axial distances of the two adjacent tunnels are 60, 60, 60, 45, 35 and 35 m, respectively. The average length, slope and orientation of these tunnels are 16.67 km, 0.365% and N58°W, respectively. The tunnels 1#, 3# and C#, with diameters of 12.4, 12.4 m and 7.2 m, respectively, are excavated by tunnel boring machine (TBM) method. By contrast, the tunnels 2# and 4# with the same horseshoe-shaped cross- section are excavated by drill & blast method, and the shape and dimensions are shown in Fig. 14(a). This method has also been used for the excavation of the two auxiliary tunnels A# and B#, whose sizes are designed as 5.5 m (width) × 5.7 m (height) and 6.0 m (width) × 6.25 m (height), respectively.

### 5.2 Geological conditions

Jinping II Hydropower Station is located on the slope of the Qinghai−Tibet Plateau to the Sichuan Basin. The altitude of Jinping Mountain varies from 4100 to 4500 m. Along the axis of the tunnel, over 75.8% of the headrace tunnel has a buried depth of more than 1700 m, and the maximum value reaches 2525 m [31,32]. As shown in Fig. 14(b), tunnels pass through various strata from the entrance to the exit, namely, Zagunao group marble, Chlorite schist, Zagunao group marble, sandstone and slate in upper Triassic, Baishan group marble and Yantang group marble [33]. More than 80% of the tunnel is surrounded by hard brittle marble and sandstone, whose average uniaxial compressive strength and tensile strength are 95−105 MPa and 3−6 MPa, respectively [34]. Literature [35] indicates that a total of 15 faults were exposed during the tunnel excavation, and their orientations are mainly NNE, NNW, NE-NEE and NW-NWW. Note that faults whose orientations along the NNE direction are consistent with the main tectonic line and extension of the Jinping Mountain. Besides, few karst caves are found in the project area, and the maximum

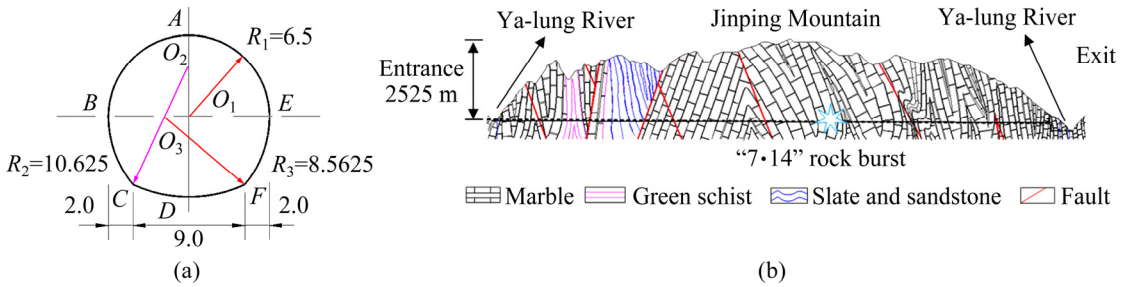


**Fig. 14** Jinping II Hydropower Station: (a) Dimensions and cross-sectional shape of headrace tunnels 2# and 4#; (b) Schematic diagram of geologic cross section (modified from Ref. [32])

water pressure is up to 10 MPa [33,36]. Influenced by the mountainous topography, various lithology and complex geological conditions, the in-situ stress fields of the headrace tunnels are very complicated. Based on the field measurement using multiple methods, it is found that the lateral stress coefficient is 0.8−1.1. Near the eastern and western ends of the tunnel, the principal stress is dominated by horizonal tectonic stress (>30 MPa). On the contrary, the vertical stress caused by gravity is the maximum principal stress in the middle of the tunnel, and the maximum value exceeds 70 MPa [37].

### 5.3 Intense rock burst and explanation

Due to the high in-situ stress, the complicated geological structure and large-scale sizes of tunnel, rock disasters, especially the rock burst, occur frequently and intensely. According to the statistics [38], 4−8 rock bursts occur every day during the tunnel excavation. A total of more than 170 rock bursts appeared on either side of the tunnel, followed by 138 rock bursts on the roof. By contrast, only few rock bursts took place at the floor. It is further found that most rock bursts occur within 40 m away from the working face in 8 days after the tunnel is excavated.

In this work, the "7·14" rock bursts occurring at Stake K9+728 m to Stake K9+766 m in the headrace tunnel 4# (see Fig. 14(b)) during its excavation was analyzed as an example. As shown in Fig. 15, after the rock burst, many rock fragments from the anchored host rock on the left sidewall of the tunnel were ejected to the right sidewall. This results in a failure zone with a depth of 6 m. It is surveyed that this part of the tunnel was in an intact marble with a thickness of 2300 m, and no obvious faults were revealed [39]. Clearly, the vertical stress is the major principal stress, and thekind of this rock burst can be categorized as strain type [40]. As can be seen in Fig. 9, when $\lambda$ is between 0.8 and 1.0, a high level of compressive stress (123.41−136.50 MPa) concentrates on the two sidewalls of the tunnel, and the maximum stress concentration factors are larger than that on the tunnel roof. This causes a large amount of energy accumulation. When it reaches a certain level or is disturbed by blasting, a rock burst is induced immediately. By contrast, the compressive stress on the tunnel floor is the smallest. Provided that $\lambda$>1, the compressive stress on the top of the tunnel is larger than that on the sidewalls, and rock burst may appear on the roof of the tunnel. To conclude, rock burst is a result of sudden release of energy accumulated inside brittle rocks under high stress, and it is most likely to occur where the excavation-induced stress is the greatest. The failure behavior and location of the tunnel under high stress coincide exactly with the numerical study (see Fig. 4).

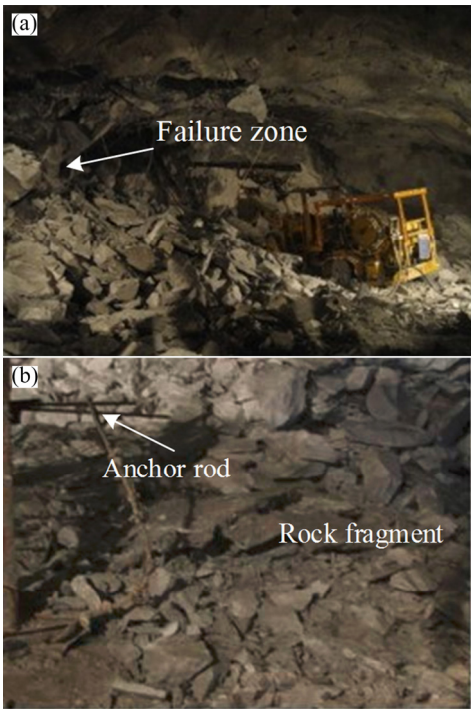


**Fig. 15** Photos of headrace tunnel 4# after rock burst [40]: (a) Rock burst failure zone; (b) Ejected anchor rod and rock fragment

## 6 Conclusions

(1) Numerical results show that the fracture around the horseshoe-shaped tunnel under uniaxial compression starts from primary-tensile crack, sidewall crack via secondary-tensile crack to shear crack. Under biaxial compression, the tensile cracks are restrained by lateral pressure, and only spalling and shear cracks appear in the models.

(2) The proposed shrinkage approximation algorithm for solving the mapping function of the horseshoe-shaped tunnel is effective, and the mapping accuracy of the tunnel shape is satisfactory when the term number of $C_m$ is 8.

(3) As the lateral stress coefficient increases, tensile stresses occurring on the roof and floor of

the tunnel decrease to 0 gradually, and then turn to compressive stresses when $\lambda$ is larger than 0.33 and 0.38, respectively. Conversely, the stress concentrated on the two sidewalls changes from compressive stress to tensile stress with the growing of the lateral stress coefficient. Additionally, as the distance from the tunnel boundary rises, the maximum tangential stress on the roof and floor gradually drops towards $\sigma_x^{\infty}$, while that on the two sides progressively falls to $\sigma_y^{\infty}$. For radial stress, the law of change is reversed.

4) The surrounding stress distributions around the tunnel can well account for the fracture mechanism. Also, the location of rock burst in the headrace tunnel 4# of the Jinping II Hydropower Station is well explained using the analytical stress solution.

## Acknowledgments

This work was supported by the Fundamental Research Funds for the Central Universities, China (No. 2021QN1010).

## References

[1] FAIRHURST C. Stress estimation in rock: A brief history and review [J]. International Journal of Rock Mechanics and Mining Sciences, 2003, 40(7/8): 957−973.

[2] WU Hao, ZHAO Guo-yan, LIANG Wei-zhang. Mechanical properties and fracture characteristics of pre-holed rocks subjected to uniaxial loading: A comparative analysis of five hole shapes [J]. Theoretical and Applied Fracture Mechanics, 2020, 105: 102433.

[3] NGUEYEP MAMBOU L L, NDOP J, NDJAKA J M B. Numerical investigations of stresses and strains redistribution around the tunnel: Influence of transverse isotropic behavior of granitic rock, in situ stress and shape of tunnel [J]. Journal of Mining Science, 2015, 51(3): 497−505.

[4] HE Man-chao. Latest progress of soft rock mechanics and engineering in China [J]. Journal of Rock Mechanics and Geotechnical Engineering, 2014, 6(3): 165−179.

[5] ZHOU Zi-long, WANG Hai-quan, CAI Xin, CHEN Lu, E Yu-de, CHENG Rui-shan. Damage evolution and failure behavior of post-mainshock damaged rocks under aftershock effects [J]. Energies, 2019, 12(23): 4429.

[6] FENG Fan, LI Xi-bing, ROSTAMI J, PENG Ding-xiao, LI Di-yuan, DU K. Numerical investigation of hard rock strength and fracturing under polyaxial compression based on mogi-coulomb failure criterion [J]. International Journal of Geomechanics, 2019, 19(4): 04019005.

[7] FIGUEIREDO B, LAMAS L, MURALHA J. Determination of in situ stresses using large flat jack tests [C]//ISRM International Symposium 2010 and 6th Asian Rock Mechanics Symposium. New Delhi: International Society for Rock Mechanics and Rock Engineering, 2010: 23−27.

[8] GE Xiu-run, HOU Ming-xun. Principle of *in situ* 3D rock stress measurement with borehole wall stress relief method and its preliminary applications to determination of in-situ rock stress orientation and magnitude in Jinping hydropower station [J]. Science China Technological Sciences, 2012, 55(4): 939−949.

[9] CAI Mei-feng, PENG Hua, JI Hong-guang. New development of hydraulic fracturing technique for in-situ stress measurement at great depth of mines [J]. Journal of University of Science and Technology Beijing, Mineral, Metallurgy, Material, 2008, 15(6): 665−670.

[10] KAISER P K, YAZICI S, MALONEY S. Mining-induced stress change and consequences of stress path on excavation stability−A case study [J]. International Journal of Rock Mechanics and Mining Sciences, 2001, 38(2):167−180.

[11] OUYANG Zhen-hua, LI Chang-hong, XU Wan-cai, LI Hao-jie. Measurements of in situ stress and mining-induced stress in Beiminghe Iron Mine of China [J]. Journal of Central South University of Technology, 2009, 16(1): 85−90.

[12] QIU Li-ming, WANG En-yuan, SONG Da-zhao, LIU Zhen-tang, SHEN Rong-xi, LV Gang-gang, XU Zhao-yong. Measurement of the stress field of a tunnel through its rock EMR [J]. Journal of Geophysics and Engineering, 2017, 14(4): 949−959.

[13] MAXWELL S C, YOUNG R P. Sequential velocity imaging and microseismic monitoring of mining-induced stress change [J]. Pure and Applied Geophysics, 1992, 139(3/4): 421−447.

[14] van POOLLEN H K. A photoelastic investigation of the relationship between stresses around mine openings and resulting failures [D]. Golden: Colorado School of Mines, 1955.

[15] LI Guo-dong, CAO Shu-gang, LUO Feng, LI Yong, WEI Ya-xing. Research on mining-induced deformation and stress, insights from physical modeling and theoretical analysis [J]. Arabian Journal of Geosciences, 2018, 11(5): 1−9.

[16] TAO Ming, ZHAO Hua-tao, LI Zhan-wei, ZHU Jian-bo. Analytical and numerical study of a circular cavity subjected to plane and cylindrical P-wave scattering [J]. Tunnelling and Underground Space Technology, 2020, 95: 103143.

[17] TAO Ming, ZHAO Rui, DU Kun, CAO Wen-zhuo, LI Zhan-wei. Dynamic stress concentration and failure characteristics around elliptical cavity subjected to impact loading [J]. International Journal of Solids and Structures 2020, 191/192: 401−417.

[18] FAN Xiang, LI Kai-hui, LAI Hong-peng, XIE Yong-li, CAO Ri-hong, ZHENG Jun. Internal stress distribution and cracking around flaws and openings of rock block under uniaxial compression: A particle mechanics approach [J]. Computers and Geotechnics, 2018, 102: 28−38.

[19] FENG Fan, CHEN Shao-jie, LI Di-yuan, HU Song-tao, HUANG Wan-peng, LI Bo. Analysis of fractures of a hard rock specimen via unloading of central hole with different sectional shapes [J]. Energy Science and Engineering, 2019, 7(6): 2265−2286.

[20] ZHAO Guang-pu, YANG Sheng-li. Analytical solutions for rock stress around square tunnels using complex variable theory [J]. International Journal of Rock Mechanics and Mining Sciences, 2015, 80: 302−307.

[21] GRM A, BATISTA M. On the coupling of analytical and FEM solution in stress analysis around the polygonal hole shape in a finite two-dimensional domain [J]. International Journal of Mechanical Sciences, 2016, 118: 254−267.
[22] PAN Zu-xing, CHENG Yuan-sheng, LIU Jun. Stress analysis of a finite plate with a rectangular hole subjected to uniaxial tension using modified stress functions [J]. International Journal of Mechanical Sciences, 2013, 75: 265−277.
[23] TRAN MANH H, SULEM J, SUBRIN D. A closed-form solution for tunnels with arbitrary cross section excavated in elastic anisotropic ground [J]. Rock Mechanics and Rock Engineering, 2015, 48(1): 277−288.
[24] LU Ai-zhong, ZHANG Ning, ZHANG Xiao-li, LU Dong-hai. Analytic method of stress analysis for an orthotropic rock mass with an arbitrary-shaped tunnel [J] International Journal of Geomechanics, 2015, 15(4): 04014068.
[25] WU Hao, KULATILAKE P H S W, ZHAO Guo-yan, LIANG Wei-zhang. Stress distribution and fracture evolution around a trapezoidal cavity in sandstone loaded in compression [J]. Theoretical and Applied Fracture Mechanics, 2019, 104: 102348.
[26] CHO N, MARTIN C D, SEGO D C. A clumped particle model for rock [J]. International Journal of Rock Mechanics and Mining Sciences, 2007, 44(7): 997−1010.
[27] WU Hao, ZHAO Guo-yan, LIANG Wei-zhang. Mechanical response and fracture behavior of brittle rocks containing two inverted U-shaped holes under uniaxial loading [J]. Applied Sciences, 2019, 9(24): 5327.
[28] CHEN Zi-yin. Analytical method of rock mechanics analysis [M]. Beijing: China Coal Industry Publishing House, 1994. (in Chinese)
[29] MUSKHELISHVILI N I. Some basic problems of the mathematical theory of elasticity [M]. Dordrecht: Springer Netherlands, 1977.
[30] LU Ai-zhong, ZHANG Lu-qing. Complex function method on mechanical analysis of underground tunnel [M]. Beijing: Science Press, 2007. (in Chinese)
[31] ZHANG Chuan-qing, FENG Xia-ting, ZHOU Hui. Estimation of in situ stress along deep tunnels buried in complex geological conditions [J]. International Journal of Rock Mechanics and Mining Sciences, 2012, 52: 139−162.
[32] SHAN Zhi-gang, YAN Peng. Management of rock bursts during excavation of the deep tunnels in Jinping II Hydropower Station [J]. Bulletin of Engineering Geology and the Environment, 2010, 69(3): 353−363.
[33] JIANG Quan, FENG Xia-ting, XIANG Tian-bing, SU Guo-shao. Rockburst characteristics and numerical simulation based on a new energy index: A case study of a tunnel at 2,500 m depth [J]. Bulletin of Engineering Geology and the Environment, 2010, 69(3): 381−388.
[34] WU Shi-yong, WANG Ge. Rock mechanical problems and optimization for the long and deep diversion tunnels at Jinping II hydropower station [J]. Journal of Rock Mechanics and Geotechnical Engineering, 2011, 3(4): 314−328.
[35] FENG Guang-liang, XIA Guo-qing, CHEN Bing-rui, XIAO Ya-xun, ZHOU Rui-chen. A method for rockburst prediction in the deep tunnels of hydropower stations based on the monitored microseismicity and an optimized probabilistic neural network model [J]. Sustainability, 2019, 11(11): 3212.
[36] LIU Fei, MA Tian-hui, TANG Chun-an, CHEN Feng. Prediction of rockburst in tunnels at the Jinping II hydropower station using microseismic monitoring technique [J]. Tunnelling and Underground Space Technology, 2018, 81: 480−493.
[37] FENG Xia-ting, ZHOU Yang-yi, JIANG Quan. Rock mechanics contributions to recent hydroelectric developments in China [J]. Journal of Rock Mechanics and Geotechnical Engineering, 2019, 11(3): 511−526.
[38] WANG Ji-min, ZENG Xiong-hui, ZHOU Ji-fang. Practices on rockburst prevention and control in headrace tunnels of Jinping II hydropower station [J]. Journal of Rock Mechanics and Geotechnical Engineering, 2012, 4(3): 258−268.
[39] MA Tian-hui, TANG Chun-an, TANG Lie-xian, ZHANG Wen-dong, WANG Long. Rockburst characteristics and microseismic monitoring of deep-buried tunnels for Jinping II Hydropower Station [J]. Tunnelling and Underground Space Technology, 2015, 49: 345−368.
[40] ZHANG Chuan-qing, FENG Xia-ting, ZHOU Hui, QIU Shi-li, WU Wen-ping. Case histories of four extremely intense rockbursts in deep tunnels [J]. Rock Mechanics and Rock Engineering, 2012, 45(3): 275−288.

# 高应力作用下硬岩马蹄形巷(隧)道破坏行为：现象和机理

吴 浩[1]，赵国彦[2]，马少维[2]

1. 中国矿业大学 矿业工程学院，徐州 221116；2. 中南大学 资源与安全工程学院，长沙 410083

**摘 要**：首先采用颗粒流程序(PFC)研究含马蹄形孔洞板状岩石模型在双轴压缩下的力学响应；其次，采用改进的复变函数法推导孔洞周边应力分布；最后，对锦屏二级水电站因岩爆引起的隧道破坏实例进行分析和讨论。结果表明，在低侧限应力作用下，孔洞周围共出现 4 种类型裂纹，即孔洞顶底板的初始拉伸裂纹、侧壁上的剥落裂缝、拐角处的次生拉伸裂纹和对角线上的剪切裂纹。随着侧限应力的增加，拉伸裂纹逐渐消失，而剥落破坏愈发严重。隧道模型的破坏现象与实际引水隧道的非常吻合，且解析获得的应力分布可以阐明裂纹的萌生机理。

**关键词**：马蹄形隧道；破裂行为；岩爆；应力分布；复变方法；颗粒流程序

**(Edited by Xiang-qun LI)**